Paleoceanography and Paleoclimatology

RESEARCH ARTICLE
10.1029/2019PA003811

# Enhanced Poleward Flux of Atmospheric Moisture to the Weddell Sea Region (ODP Site 690) During the Paleocene-Eocene Thermal Maximum

**Reinhard Kozdon[1], Donald E. Penman[2], D. C. Kelly[3], J. C. Zachos[4], John H. Fournelle[3], and J. W. Valley[5]**

[1]Lamont-Doherty Earth Observatory of Columbia University, Palisades, NY, USA, [2]Department of Geology and Geophysics, Yale University, New Haven, CT, USA, [3]Department of Geoscience, UW-Madison, Madison, WI, USA, [4]Department of Earth and Planetary Sciences, UC-Santa Cruz, Santa Cruz, CA, USA, [5]WiscSIMS, Department of Geoscience, UW-Madison, Madison, WI, USA

**Key Points:**
- We present the first Mg/Ca-based sea-surface temperature record for the iconic PETM section from Site 690 (Weddell Sea)
- Our results indicate delayed, but sustained, reduction in sea-surface salinity at Site 690 during the PETM
- The hydrological cycle perturbation manifests as an enhanced poleward flux of atmospheric moisture during the PETM

**Supporting Information:**
- Supporting Information S1
- Table S1
- Table S2
- Table S3
- Table S4
- Table S5

**Correspondence to:**
R. Kozdon,
rkozdon@ldeo.columbia.edu

**Citation:**
Kozdon, R., Penman, D. E., Kelly, D. C., Zachos, J. C., Fournelle, J. H., & Valley, J. W. (2020). Enhanced poleward flux of atmospheric moisture to the Weddell Sea region (ODP site 690) during the Paleocene-Eocene thermal maximum. *Paleoceanography and Paleoclimatology*, *35*, e2019PA003811. https://doi.org/10.1029/2019PA003811

Received 8 NOV 2019
Accepted 15 APR 2020
Accepted article online 29 APR 2020

©2020. American Geophysical Union. All Rights Reserved.

**Abstract** Earth's hydrological cycle was profoundly perturbed by massive carbon emissions during an ancient (56 Ma) global warming event referred to as the Paleocene-Eocene thermal maximum (PETM). One approach to gaining valuable insight into the response of the hydrological cycle is to construct sea-surface salinity (SSS) records that can be used to gauge changes in the rates of evaporation and precipitation during the PETM in such climatically sensitive areas as the circum-Antarctic region. Here, we pair oxygen isotope ($\delta^{18}O$) and magnesium-calcium (Mg/Ca) measurements to reconstruct PETM sea-surface temperatures (SSTs) and $\delta^{18}O$ composition of seawater ($\delta^{18}O_{sw}$) at austral Site 690 (Weddell Sea). Several discrepancies emerge between the $\delta^{18}O$- and Mg/Ca-based SST records, with the latter indicating that the earliest PETM was punctuated by a short-lived ~4°C increase in local SSTs. Conversion of the $\delta^{18}O_{sw}$ values to SSS reveals a ~4 ppt decrease ~50 ka after peak PETM warming at Site 690. This negative SSS ($\delta^{18}O_{sw}$) anomaly coincides with a prominent minimum in the planktic foraminifer $\delta^{18}O$ record published for the Site 690 PETM section. Thus, our revised interpretation posits that this $\delta^{18}O$ minimum signals a decrease in surface-ocean $\delta^{18}O_{sw}$ fostered by a transient increase in mean annual precipitation in the Weddell Sea region. The results of this study corroborate the view that the poleward flux of atmospheric moisture temporarily increased during a distinctive stage of the PETM.

## 1. Introduction

The series of transient global warming events superimposed upon the long-term greenhouse climate state of the early Paleogene (~65–39 Ma) are geological analogs for gauging the future environmental consequences of unabated greenhouse gas emissions (e.g., Zachos et al., 2008; Zeebe et al., 2009; Zeebe & Zachos, 2013). The most prominent of these "thermal maxima" occurred ~56 Ma (Zeebe & Lourens, 2019) and is referred to as the Paleocene-Eocene thermal maximum or PETM. Hallmarks of the PETM in deep-sea records are abrupt decreases in the oxygen ($\delta^{18}O$) and carbon isotope ($\delta^{13}C$) compositions of foraminifer calcite (e.g., Kennett & Stott, 1991; Zachos et al., 2001) and a sharp decline in sedimentary calcite content (Dickens et al., 1997; Thomas et al., 1999). Together, these lines of evidence reflect ~4–5°C of ocean warming coupled with a brief pulse of intense carbonate dissolution driven by the geologically rapid release of massive quantities of $\delta^{13}C$-depleted carbon (e.g., Aze et al., 2014; Babila et al., 2016; Babila et al., 2018; DeConto et al., 2012; Dickens et al., 1995; Frieling et al., 2017; Higgins & Schrag, 2006; Jones et al., 2013; Penman et al., 2014; Svensen et al., 2004; Zachos et al., 2003; Zachos et al., 2005; Zachos et al., 2006; Zeebe et al., 2008).

The source(s) for carbon input during the PETM is debated (e.g., McInerney & Wing, 2011), but there is general consensus that many aspects of the PETM climatic and carbon cycle responses provide contextual constraints on ocean-climate change predicted to unfold in the coming centuries (Zeebe & Zachos, 2013). In theory, rising surface temperatures should accelerate and intensify the hydrological cycle (Clementz & Sewall, 2011; Held & Soden, 2000, 2006); hence, the greenhouse climate state of the PETM is thought to have been broadly associated with a more humid atmosphere (Bowen et al., 2004; Tipple et al., 2011). There is now a large body of evidence to indicate that the response of the hydrological cycle entailed a high degree of regional and temporal variability (Carmichael et al., 2017; Clechenko et al., 2007; Egger et al., 2003; Foreman

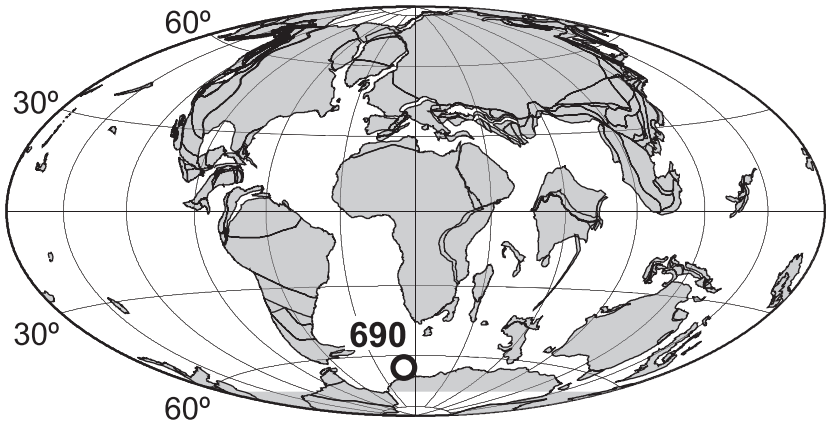


**Figure 1.** Early Eocene paleogeography and location of Site 690, Weddell Sea (map modified from the ocean drilling stratigraphic network, ODSN, compiled using data files from (Hay et al., 1999)).

et al., 2012; Handley et al., 2012; John et al., 2012; Kraus & Riggins, 2007; Larrasoaña et al., 2012; Pagani et al., 2006; Pujalte et al., 2019; Schmitz & Pujalte, 2007; Wing et al., 2005). Nonetheless, a first-order feature of the PETM hydrological cycle that was more global in scope appears to have been an increase in meridional (equator-to-pole) transport of atmospheric water vapor (e.g., Huber & Goldner, 2012; Pagani et al., 2013; Pierrehumbert, 2002). Support for such an increase in poleward moisture transport is provided by micropaleontological and *n*-alkane hydrogen isotope records indicating reduced sea-surface salinities in the central Arctic Ocean during the PETM (Pagani et al., 2006; Sluijs et al., 2008).

In this study, we build upon the foundation laid by previous studies in an effort to better understand how the poleward flux of water vapor changed in response to rapid carbon input during the PETM. To this end, paired $\delta^{18}O$ and Mg/Ca ratios measured from planktic foraminifer shells are used to generate parallel records of sea-surface temperature (SST) and seawater oxygen isotope composition ($\delta^{18}O_{sw}$) for the PETM section recovered at Ocean Drilling Program (ODP) Site 690 (Figure 1). This approach to reconstructing spatiotemporal variation in the hydrological cycle is predicated upon observed covariance between meridional gradients in surface $\delta^{18}O_{sw}$ and sea-surface salinity (SSS) in the modern ocean as both seawater properties are a function of differences in evaporation and precipitation (e.g., Schmitt, 1995). Culturing experiments have shown that the oxygen isotope composition of planktic foraminifer shells ($\delta^{18}O_{shell}$) is dependent upon both $\delta^{18}O_{sw}$ and calcification temperature (e.g., Bemis et al., 1998; Shackleton, 1967), whereas the magnesium content of their shells increases exponentially with increasing temperatures (e.g., Lea et al., 1999). Thus, both SSTs and surface $\delta^{18}O_{sw}$ can be determined by measuring $\delta^{18}O_{shell}$ and Mg/Ca ratios in tandem from fossil planktic foraminifers (e.g., Anand et al., 2003; Anand et al., 2008; Dahl & Oppo, 2006; Elderfield & Ganssen, 2000; Flower et al., 2004).

The PETM was first characterized using foraminifer stable isotope records constructed for the Site 690 section (Kennett & Stott, 1991), so this stratigraphic section has played a central role in shaping our perception of the PETM. Yet, a complementary SST record based on planktic foraminifer Mg/Ca ratios has hitherto been lacking for this iconic PETM section. We address this shortcoming by reporting two parallel planktic foraminifer Mg/Ca ratio records that were independently generated using different analytical techniques, which show similar values and trends through the Site 690 PETM section. Added incentive for

targeting the Site 690 section is that it represents one of only a handful of PETM records from the circum-Antarctic region (Figure 1) and as such is geographically well positioned for monitoring changes in the poleward flux of atmospheric moisture during the PETM. This is the case because Rayleigh distillation renders the $\delta^{18}O$ of atmospheric water vapor (and precipitation) extremely $^{18}O$-depleted relative to that of the surface ocean (Craig & Gordon, 1965). Thus, a perturbation to the global hydrological cycle resulting in enhanced poleward transport of atmospheric moisture should be signaled by a reduction in surface $\delta^{18}O_{sw}$ (and SSS) at Site 690. It is for this reason that the prominent minimum seen in the published (Kennett & Stott, 1991) planktic foraminifer $\delta^{18}O_{shell}$ record about midway through the CIE interval in the Site 690 PETM section is of particular interest to this study.

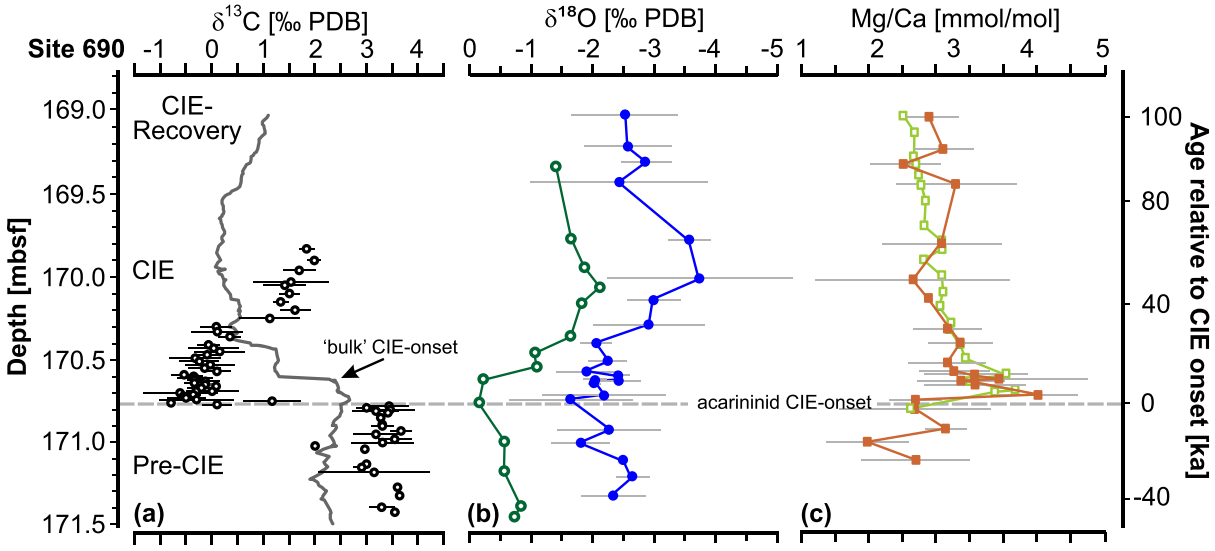


**Figure 2.** Parallel chemostratigraphies for the Site 690 PETM section. Data plotted against core depth (meters below seafloor, mbsf) and relative (± ka) to CIE onset in the planktic foraminifer (acarininid) $\delta^{13}C$ record. (a) Bulk-carbonate (solid line) and acarininid (open circles) $\delta^{13}C$ records of the carbon isotope excursion (CIE). Acarininid record constructed using mean values of published (Thomas et al., 2002) single-shell data, error bars represent ±2 SEM for each sample. Note: Acarininid shells displaced by sediment mixing were excluded, and CIE onset in bulk-carbonate record occurs 14 cm above its position in the acarininid record (Hupp et al., 2019). (b) Parallel planktic foraminifer $\delta^{18}O$ records, one constructed with in situ SIMS values (blue, filled circles) and the other with values obtained by conventional multi-shell acid solution techniques (green, open circles) (Kennett & Stott, 1991). Error bars in the SIMS-based $\delta^{18}O$ record represent ±2 SEM for each sample. (c) Complementary acarininid Mg/Ca ratio records, one constructed with in situ EPMA values (brown, filled squares, with error bars connoting ±2 SEM for each sample) and the other with values obtained by conventional, multi-shell ICP-MS analysis (light green, open squares). Error bars on in situ values are large due to inter- and intrashell variability in Mg/Ca; however, average values for each core sample delineate the same trends as conventional, multi-shell ICP-MS measurements.

## 2. Material and Methods

### 2.1. Study Site, Materials, and Chronostratigraphic Framework

Site 690 was drilled ~400 km offshore of Antarctica (65°09′S, 01°12′E) along the southwestern flank of Maud Rise in the Weddell Sea at a water depth of 2,940 meters (Barker & Kennett, 1988). Benthic foraminifer assemblages indicate a lower bathyal (~1900 m) paleo-water depth during the late Paleocene (Thomas, 1990). This relatively shallow bathymetric setting is thought to have helped minimize carbonate dissolution at Site 690; nevertheless, sedimentary calcite content decreases at the base of the section (Farley & Eltgroth, 2003; Röhl et al., 2000). The Site 690 PETM section has been studied extensively and is well-constrained by microfossil biostratigraphies (Bralower, 2002; Kelly, 2002) and foraminifer stable isotope ($\delta^{13}C$, $\delta^{18}O$) records (Kennett & Stott, 1991; Thomas et al., 2002).

The highly-resolved bulk-carbonate $\delta^{13}C$ ($\delta^{13}C_{bulk}$) stratigraphy published for the Site 690 section (Bains et al., 1999), as well as complementary foraminifer stable isotope records (Kennett & Stott, 1991; Thomas et al., 2002), served to guide sample selection. Accordingly, the study section (~171.12 to 169.04 meters below seafloor, mbsf) comprises a stratigraphic series of 23 core samples spanning the pre-CIE to CIE transition and extending upwards into the lower part of the CIE recovery of the Site 690 PETM section (see supporting information Table S1). The bulk-sediment samples were disaggregated using a pH-buffered sodium hexametaphosphate hydrogen peroxide (30%) solution, wet sieved (>63 μm), rinsed with distilled water, and oven-dried (30°C) overnight. Whenever possible, roughly 20 shells of the planktic foraminifer species *Acarinina soldadoensis* were handpicked from narrow size ranges (250–300 μm or 300–355 μm) of each core sample. The stable isotope signature of *A. soldadoensis* indicates that this species harbored photosymbionts and inhabited the euphotic zone of the oceanic mixed layer (Quillévéré et al., 2001), so its depth ecology is well suited for reconstructing surface-ocean conditions.

The Site 690 PETM stratigraphy has been calibrated against an astronomically tuned age model, with the resulting ages being reported relative to the CIE onset in the $\delta^{13}C_{bulk}$ record (Röhl et al., 2007). However, a recent study (Hupp et al., 2019) has shown that size-dependent sediment mixing has resulted in a ~14-

cm stratigraphic offset between the core depths where the CIE onset is first registered by planktic foraminifer shells (*Acarinina* spp., >250 μm) and bulk-carbonate samples (Figure 2a). Based on the sedimentation rates reported by Röhl et al. (2007), we estimate that this stratigraphic offset equates to a temporal discrepancy of ~7.31 ka. Our $\delta^{18}O$ and Mg/Ca ratio records were compiled from the same planktic foraminifer genus (*Acarinina*) and size fraction (>250 μm) used to construct the high-resolution, planktic foraminifer $\delta^{13}C$ record for the Site 690 PETM section (Thomas et al., 2002). As a result, we used the core depth (170.78 m) of the CIE onset in the *Acarinina* spp. $\delta^{13}C$ record ($\delta^{13}C_{acarininid}$) as our chronostratigraphic reference point in order to maintain internal consistency. An added constraint on sample selection is that the response of planktic foraminifers to PETM conditions entailed a high degree of taxonomic turnover at Site 690, with *A. soldadoensis* temporarily disappearing from the overlying CIE recovery interval (Kelly et al., 2005).

In short, the geochemical records herein reported begin ~34 cm below the stratigraphic level of the CIE onset in the $\delta^{13}C_{acarininid}$ record and extend up-section across the pre-CIE to CIE transition through the interval over which the prominent minimum in the planktic foraminifer $\delta^{18}O_{shell}$ record occurs in the Site 690 PETM section (Figure 2). We assigned the CIE onset in the $\delta^{13}C_{acarininid}$ record an age of 0.0 ka and adjusted the previously reported ages for our samples accordingly with all sample ages being reported relative (±ka) to the CIE onset in the $\delta^{13}C_{acarininid}$ record. Our revised age model indicates that the study section initiates at −17.36 ka and ends at +101.85 ka relative to the CIE onset in the $\delta^{13}C_{acarininid}$ record (Table S1).

### 2.2. Foraminifer Preservation

All planktic foraminifer shells from the PETM section of Site 690 feature a "frosty" (opaque) hue when observed under reflected light, with acarininid shells possessing thickened blade-like structures (termed muricae, Blow, 1979) protruding from their surfaces. These are the telltale signs of post-depositional diagenesis (Kozdon et al., 2013; Pearson et al., 2001; Sexton et al., 2006), which is problematic for conventional planktic foraminifer $\delta^{18}O_{shell}$ analyses requiring acid-digestion of entire shells. In addition, post-depositional diagenesis tends to smooth long-term paleoclimate trends in planktic foraminifer $\delta^{18}O_{shell}$ records (Killingley, 1983) and has demonstrably attenuated the amplitude of the negative $\delta^{18}O_{shell}$ excursion signaling PETM conditions at some sites (Kozdon et al., 2013). In this study, we attempt to minimize the unwanted effects of diagenetic overprinting by performing in situ analyses of better-preserved domains within individual foraminifer shells. Specifically, previous study has shown that the basal areas of muricae contain no mural pores, making these minute domains less susceptible to diagenesis and ideal targets for in situ measurements of both $\delta^{18}O$ and Mg/Ca ratios (Kozdon et al., 2013). This approach allows for the selection of better-preserved domains as well as the acquisition of both proxies within the same homologous domain of each shell. Conventional "solution-phase" measurements of Mg/Ca ratios were also performed in parallel for comparison with in situ measurements of Mg/Ca ratios.

### 2.3. In situ $\delta^{18}O$ and Mg/Ca Measurements

Detailed descriptions of $\delta^{18}O$ measurements in foraminifer shells by secondary ion mass spectrometry (SIMS) are published elsewhere (Kozdon et al., 2009; Kozdon et al., 2011). In short, acarininid shells were cast in epoxy, ground to midsection, and imaged by SEM to identify suitable domains for analysis. In situ $\delta^{18}O$ data were acquired in the WiscSIMS Laboratory at the Department of Geoscience, UW-Madison, using a CAMECA IMS-1280 large radius multicollector SIMS (Kita et al., 2009; Valley & Kita, 2009) with analytical conditions similar to those reported by Kozdon et al. (2011). Depending on the size of the target, samples were analyzed with a 10 μm or 3 μm primary beam (Table S2). Four consecutive measurements of UWC-3 calcite standard ($\delta^{18}O$ = 12.40‰ Vienna standard mean ocean water; VSMOW; Kozdon et al., 2009) were performed before and after every set of typically 10 sample analyses. The average analytical precision (reproducibility) for 10 μm beam conditions was 0.3‰ (±2 SD, spot-to-spot) and ± 0.7‰ for analysis performed with a 3 μm primary beam. Every polished acarininid shell featured several suitable domains for in situ measurements. We found that intrashell $\delta^{18}O$ variation of these domains is typically within analytical error; thus, only 1–2 in situ SIMS $\delta^{18}O$ measurements were performed in each acarininid shell. After SIMS $\delta^{18}O$ measurements, the appearance of each analysis pit was assessed by SEM imaging. We consider $\delta^{18}O$ data from "irregular" pits (Cavosie et al., 2005) overlapping epoxy resin, cracks, and cavities as being possibly compromised, and values from these measurements were excluded from the data set.

In situ Mg/Ca ratios were acquired from ~3-μm diameter spots within the muricae bases of the acarininid shells using a CAMECA SX-51 electron microprobe at the UW-Madison Department of Geoscience with analytical conditions similar to those previously reported (Kozdon et al., 2013). Whenever possible, Mg/Ca analyses were made adjacent to the SIMS analysis pits or in comparable domains within the same chamber. Only EPMA analytical totals of 98.5–100.5 wt.% were considered acceptable (Table S3). As previously reported by Nuernberg (1995), Mg/Ca measurements in planktic foraminifer shells by EPMA exhibit a substantial degree of intrashell variation due to various processes affecting biocalcification (e.g., Bentov & Erez, 2006; Eggins et al., 2003). Thus, whenever possible, multiple Mg/Ca measurements were made in each acarininid shell and used to calculate the average value of each specimen.

For comparative purposes, a parallel whole-shell planktic foraminifer Mg/Ca record was constructed independently (Table S4). From each sample, 15–25 shells of *A. soldadoensis* (250–300 μm size fraction) were crushed and cleaned with a reductive-oxidative treatment (Boyle & Keigwin, 1985 as revised by Martin & Lea, 2002] prior to being dissolved in 0.075 N $HNO_3$. The Mg/Ca ratios were measured using a Finnigan Element XR inductively coupled plasma mass spectrometer (ICP-MS) housed at the University of California Santa Cruz and following the methods of Brown et al. (2011). Based on replicate measurements of an in-house carbonate standard, external precision on calcite Mg/Ca ratios is 2% (RSD).

### 2.4. Calculation of Mg/Ca Temperature Anomalies

Pre-CIE baseline conditions were determined by EPMA measurements of 19 shells from four core samples ranging from 170.81 to 171.12 mbsf (−1.53 to −17.36 ka relative to the CIE onset), with an average Mg/Ca ratio of 2.63 mmol/mol (Table S5). The PETM is associated with a significant (~0.3 pH units) drop in ocean pH (e.g. Babila et al., 2018; Gutjahr et al., 2017; Penman et al., 2014), which is estimated to increase the Mg/Ca ratios of foraminifer shells by about 15% (Evans et al., 2016). The $\delta^{11}B$ and B/Ca records by Penman et al. (2014) indicate an abrupt and sustained acidification of the upper ocean coincident with the onset of the PETM. Therefore, all Mg/Ca ratios above the CIE onset (1.57 ka to 101.85 ka after CIE onset, Table S1) were adjusted by 15% to account for the effect ocean acidification on foraminifer Mg/Ca, whereas pre-CIE Mg/Ca ratios remained uncorrected.

The temperature dependence of foraminifer Mg/Ca to temperature is described by the general equation (e.g., Anand et al., 2003; Lea et al., 1999):

$$Mg/Ca_{shell} = B \times \exp^{A \times T} \quad (1)$$

where Mg/Ca is in mmol/mol, $T$ is the calcification temperature in °C, $A$ is the exponential constant for temperature sensitivity, and $B$ is the pre-exponential constant. A range of values for $B$ and $A$ has been published based on shells from plankton tows, sediment traps, core tops, or culture experiments (e.g., Anand et al., 2003; Elderfield & Ganssen, 2000; Gray et al., 2018; Lea et al., 1999; Rosenthal et al., 1997). For the calculation of relative temperature changes with respect to pre-CIE conditions, the pre-exponential constant $B$ is not required. Accordingly, Mg/Ca temperature anomalies were calculated using the equation of Zachos et al. (2003):

$$\Delta T = \frac{1}{A} \ln \left[ \frac{C}{100} + 1 \right] \quad (2)$$

where $\Delta T$ is the relative change in temperature (°C) and $C$ is the percentage change in Mg/Ca with respect to the mean pre-CIE baseline Mg/Ca value of 2.63 mmol/mol.

Use of planktic foraminifer Mg/Ca ratios to calculate SSTs must take into account the Mg/Ca ratio of past seawater ($Mg/Ca_{sw}$). Coupled clumped-isotope and Mg/Ca ratio measurements of foraminifer shells from a set of globally distributed sites suggest that the Mg/Ca ratio of early Eocene seawater was ~2 mol/mol, ~40% of modern (Evans et al., 2018). Comparably lower values of early Eocene $Mg/Ca_{sw}$ were determined by analyses of calcite veins that precipitated from seawater-derived fluids in ocean ridge flank basalts (Coggon et al., 2010). In addition, the response of foraminifer Mg/Ca to lower $Mg/Ca_{sw}$ is nonlinear (Evans et al., 2015; Evans et al., 2016; Segev & Erez, 2006), and the exponential constant $A$ for lower $Mg/Ca_{sw}$ needs to be determined. As the planktic foraminifer species used in this study is extinct, we used

the adjustment for lower $Mg/Ca_{sw}$ reported by Evans, Brierley, et al. (2016), which is based on the response of cultured specimens of the modern planktic foraminifer species *Globigerinoides ruber* to variations in $Mg/Ca_{sw}$:

$$A = -0.0029\, xMg/Ca_{sw}^{2} + 0.032 \text{ x } Mg/Ca_{sw} \quad (3)$$

With an early Eocene $Mg/Ca_{sw}$ value of 2.0 mol/mol, the exponential constant $A$ calculated by equation 3 is 0.056. This value is used in equation 2 to calculate Mg/Ca temperature anomalies.

### 2.5. Calculation of $\delta^{18}O$-Temperature, $\delta^{18}O_{sw}$ Composition, and Salinity Anomalies

For the calculation of $\delta^{18}O$-based temperature anomalies, pre-CIE baseline conditions were determined by averaging in situ $\delta^{18}O$ analyses in 13 shells from four core samples ranging from 170.81 to 171.12 mbsf (−1.53 to −17.36 ka relative to the CIE onset) with an average $\delta^{18}O$ value of −2.21‰ (Table S5). Similar to Mg/Ca, planktic foraminifer $\delta^{18}O$ values are sensitive to changes in ocean pH. Therefore, $\delta^{18}O_{SIMS}$ values from shells sampled within the CIE interval (+1.57 ka to +101.85 ka after CIE onset, Table S5) were adjusted by 0.27‰ (Uchikawa & Zeebe, 2010) to account for the abrupt and sustained drop of 0.3 pH units after the CIE onset (sensitivity of −0.89‰/pH unit). Pre-CIE $\delta^{18}O$ values remained unadjusted. The relationship between ocean pH and planktic foraminifer $\delta^{18}O$ has been robustly characterized for only two modern species, and their sensitivities vary significantly (−0.89‰/pH unit and −2.51‰/pH unit, Spero et al., 1997; Uchikawa & Zeebe, 2010). We therefore performed additional calculations using the higher sensitivity of −2.51‰/pH unit and show these results in the Supplementary Material (Figure S1, SOM). The $\delta^{18}O$ temperature anomaly relative to the pre-CIE baseline was calculated using a $\Delta\delta^{18}O_{calcite}/\Delta T$ relation of −0.213‰/°C (e.g., Zachos et al., 2003).

Differences between the $\delta^{18}O_{SIMS}$ and Mg/Ca-based SST anomaly records suggest local changes in surface $\delta^{18}O_{sw}$ driven by secular variation in the precipitation-evaporation balance at Site 690. We therefore used the $\Delta\delta^{18}O_{shell}/\Delta T$ relation (−0.213‰/°C) to convert these differences to expected changes in surface $\delta^{18}O_{sw}$ composition. For example, if the SST anomalies calculated independently from Mg/Ca and $\delta^{18}O$ differ by 1°C, past surface $\delta^{18}O_{sw}$ needs to be adjusted by 0.213‰ so that both temperature anomalies feature the same values with respect to pre-CIE baseline conditions. The adjustment to $\delta^{18}O_{sw}$ (0.213‰) used to reconcile the difference between $\delta^{18}O_{SIMS}$ and Mg/Ca-based SST anomaly records is then converted to change in sea surface salinity (SSS). However, the $\Delta\delta^{18}O_{sw}/D_{salinity}$ relation is not well constrained for early Eocene high latitude oceans and varies from 0.25‰/salinity unit to 0.50‰/salinity unit (Zachos et al., 2003). Depending on the $\Delta\delta^{18}O_{sw}/D_{salinity}$ relation, the adjustment of 0.213‰ to $\delta^{18}O_{sw}$ corresponds to a change in SSS between ~0.45 and ~0.9 psu. We therefore use both of the aforementioned $\Delta\delta^{18}O_{sw}/D_{salinity}$ relations to delimit SSS variation expressed in our $\delta^{18}O_{sw}$ record.

Planktic foraminifer Mg/Ca ratios are also sensitive to salinity, showing a ~3% to 5% decrease in Mg/Ca with for each unit decrease in salinity (e.g., Hönisch et al., 2013). Thus, an adjustment for salinity should be considered as uncorrected Mg/Ca values may cause a significant overestimation of the salinity shift. We caution, however, that such a salinity correction involves a degree of circular reasoning since salinity variation was initially based on paired $\delta^{18}O$:Mg/Ca analyses. With this caveat in mind, we adjusted our planktic foraminifer Mg/Ca ratios to more fully appreciate how changes in salinity might influence our Mg/Ca-based SST and $\delta^{18}O_{sw}$ reconstructions. This "sensitivity test" was carried out using an empirically derived relation ($\Delta Mg/Ca = 4\%$ per salinity unit) for salinity effect (Hönisch et al., 2013) and the average salinities (i.e., mean of the "salinity field" defined by the $\Delta\delta^{18}O_{sw}/D_{salinity}$ relation ranging from 0.25‰/salinity unit to 0.50‰/salinity unit) that were initially computed for each core sample without any salinity correction to iteratively adjust our measured Mg/Ca ratios. The resulting "salinity-corrected" Mg/Ca ratios were then used to recalculate the Mg/Ca-temperature anomaly record. The differences between the $\delta^{18}O_{SIMS}$ and salinity-corrected Mg/Ca SST anomalies were then used to recalculate $\delta^{18}O_{sw}$ and SSS anomalies (Table S5). The salinity correction for Mg/Ca reduces the amplitude of the SSS anomaly by about 40%.

## 3. Results

Given the uncertainties surrounding both the $\delta^{18}O$ and Mg/Ca ratio records, we opted not to report absolute values for the various environmental parameters (SST, $\delta^{18}O_{sw}$, and SSS) and instead describe environmental

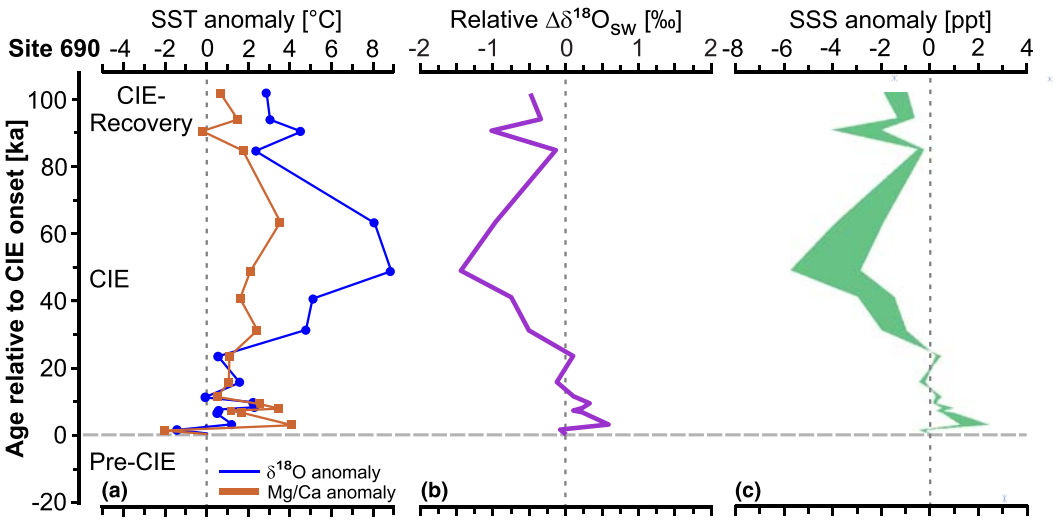


**Figure 3.** Secular variation in sea-surface properties during the PETM at Site 690 as expressed relative to pre-CIE background conditions. (a) Parallel sea-surface temperature anomaly records constructed with planktic foraminifer in situ $\delta^{18}O_{SIMS}$ data assuming a constant $\delta^{18}O_{sw}$ value (blue), and in situ Mg/Ca measurements (brown). The $\delta^{18}O_{SIMS}$ anomaly record corrected for pH drop that occurred after the CIE onset, and the Mg/Ca anomaly record is adjusted for lower Eocene seawater Mg/Ca, pH, and salinity (see section 2.5 for more details). (b) Changes in $\delta^{18}O_{sw}$ computed using the differences between the $\delta^{18}O_{SIMS}$ SST anomaly record and the Mg/Ca SST anomaly record. (c) Sea-surface salinity anomalies relative to the pre-CIE baseline calculated using a range of $\Delta\delta^{18}O_{sw}$/Δsalinity relations (0.5‰/salinity unit and 0.25‰/salinity unit). Horizontal dashed line (gray) = CIE onset in acarininid $\delta^{13}C$ record. Vertical dashed lines (gray) = mean baseline for pre-CIE background values.

change during the PETM as "anomalies" *relative* to the pre-CIE baseline conditions. With this being said, we note that the $\delta^{18}O_{SIMS}$ and published acarininid $\delta^{18}O_{shell}$ records (Kennett & Stott, 1991) delineate grossly similar trends (Figure 2b), but the $\delta^{18}O_{SIMS}$ values are, on average, ~1‰ lower than corresponding $\delta^{18}O_{shell}$ values. Owing to the frosty appearance of the acarininid shells, we attribute this systematic offset to measurement of $^{18}O$-enriched diagenetic calcite by conventional whole-shell gas-source mass spectrometry, although inter-instrument $\delta^{18}O$ differences cannot be ruled out (e.g., Wycech et al., 2018). The $\delta^{18}O_{SIMS}$ and $\delta^{18}O_{shell}$ records show quasi-simultaneous shifts toward lower values just above the CIE onset and feature minima ($\delta^{18}O_{SIMS}$: −3.8‰, $\delta^{18}O_{shell}$: −2.2‰) ~50 ka after the CIE onset. This same interval also exhibits the largest $\delta^{18}O_{SIMS\text{-}shell}$ offset (approaching 1.5‰) between these two analytical approaches (Figure 2b). The total amplitude of the $\delta^{18}O$ decrease is ~2‰ and ~2.5‰ in the $\delta^{18}O_{shell}$ and $\delta^{18}O_{SIMS}$ records, respectively. Starting at about +60 ka after the CIE onset, $\delta^{18}O$ values in both records steadily increase back toward pre-CIE values before ending near the base of the CIE recovery interval (Figure 2b).

The two parallel Mg/Ca records show similar values and trends (Figure 2c), thereby precluding an inter-instrument or method-related bias between the in situ EPMA and conventional ICP-MS measurements. Both of the Mg/Ca records feature an abrupt, but short-lived, ~2 mmol/mol increase immediately above the level of the CIE onset that is not accompanied by a decrease in the $\delta^{18}O_{SIMS}$ and $\delta^{18}O_{shell}$ records (Figures 2b and 2c). The stratigraphic expression of this transient increase differs slightly in the two Mg/Ca records with the conventional ICP-MS record featuring a "double peak" that is less clearly defined and somewhat concatenated in the EPMA-derived record (Figure 2c). This minor discrepancy notwithstanding, Mg/Ca ratios in both records subsequently decline to values (~2.5 mmol/mol) approaching the pre-CIE baseline and remain relatively invariant over the very interval in which the minima in the $\delta^{18}O_{shell}$ and $\delta^{18}O_{SIMS}$ records occur (Figures 2b and 2c).

## 4. Discussion

### 4.1. Local Sea-Surface Temperature Anomaly at Site 690

The significance of the differences between the $\delta^{18}O_{SIMS}$ and Mg/Ca records becomes more evident when the two proxies are used to generate separate SST-anomaly records (Figure 3a). The $\delta^{18}O$ composition of foraminifer shells is a function of temperature and ambient seawater $\delta^{18}O_{sw}$, with rates of

precipitation/evaporation (i.e., salinity effect) and changes in continental ice volume being the primary controls on $\delta^{18}O_{sw}$ (e.g. Emiliani, 1955; Shackleton, 1974). The latter factor, ice volume effect, is discounted owing to the absence of large continental ice sheets during the time period encompassing the PETM (Francis, 1988). Thus, after adjusting measured $\delta^{18}O$ values from within the CIE interval by 0.27‰ to account for a drop of ~0.3 units in ocean pH (Gutjahr et al., 2017; Penman et al., 2014; Uchikawa & Zeebe, 2010), the $\delta^{18}O$-based temperature anomalies were calculated using the $\Delta\delta^{18}O_{shell}/\Delta T$ relation of −0.213°C and assuming that local surface $\delta^{18}O_{sw}$ remained constant (Shackleton & Kennett, 1975; Zachos et al., 2001). Likewise, the use of Mg/Ca ratios as an independent proxy for SST is complicated by secular variation in the Mg/Ca ratio of seawater. Most reconstructions indicate that the Mg/Ca ratio of seawater has increased over the Cenozoic, and early Eocene values for $Mg/Ca_{sw}$ were possibly as low as 2.0 mol/mol (Coggon et al., 2010; Evans et al., 2018). The response of foraminifer Mg/Ca to lower seawater Mg/Ca is nonlinear, and the pre-exponential constant of the Mg/Ca temperature equation needs to be adjusted accordingly (Evans, Brierley, et al., 2016). In addition, the pH drop of 0.3 units could have resulted in a 15% increase in foraminifer Mg/Ca (Evans et al., 2015). Therefore, the Mg/Ca temperature anomaly record (Figure 3a) is adjusted for lower Eocene seawater Mg/Ca and a ~0.3 drop in ocean pH (Table S5). An additional adjustment for the effects of salinity on foraminifer Mg/Ca ratios was also applied (see section 2.5 for more details).

Major discrepancies in the timing and amplitude of *peak* PETM warming are evident between the two SST anomaly records even after adjusting both the $\delta^{18}O$ and Mg/Ca records for the effects of various non-thermal factors (Figure 3a). Peak warming in the $\delta^{18}O_{SIMS}$ record is signaled by an apparent ~9°C anomaly at +50 ka after the CIE onset, whereas peak warming in the in situ Mg/Ca record is signaled by an abrupt ~4°C increase in SSTs just after the CIE onset at +3.13 ka. The curious "double peak" of the SST anomaly delineated by both of our Mg/Ca records could be construed as indicating that the earliest stages of the PETM entailed two pulses of ~4°C warming, one just after the CIE onset (~+3 ka) and a second at about +8 ka (Figure 3a). However, a similar double peak in warming has not been seen in other pelagic PETM sections; hence, we cannot rule out the possibility that this curious feature of our Mg/Ca records may be an artifact of sediment mixing processes at Site 690 (e.g., Hupp et al., 2019; Kirtland Turner et al., 2017; Thomas et al., 2002). After this brief increase in SSTs, Mg/Ca-based temperatures return to near pre-CIE values at +11.58 ka, followed by a slight increase (~2–3°C above pre-CIE condition) over the interval (+30 to +80 ka) in which apparent peak warming is signaled by the $\delta^{18}O_{SIMS}$ minimum (Figure 3a).

The amplitude of the local SST anomaly (4–5°C) registered by the Mg/Ca record is only about half of that inferred (~9°C) from the published Site 690 $\delta^{18}O_{shell}$ record and falls at the lower end of estimates (~5–7°C) obtained from an organic-based SST proxy ($TEX_{86}$) record generated for another PETM section in the Southern Ocean (Sluijs et al., 2011). Instead, our estimate of 4–5°C warming is more comparable in scale to SST anomalies reported for PETM sections from tropical (Aze et al., 2014; Zachos et al., 2003) and Arctic (Sluijs et al., 2006) regions and is consonant with the estimated global mean surface temperature anomaly (4–5°C) for the PETM (Jones et al., 2013). An interesting corollary to our estimate for peak warming (~4–5°C) at Site 690 is that it contradicts the notion of "polar amplification" in the absence of ice-albedo effects during the PETM (e.g., Sluijs et al., 2006).

The absence of polar amplification in our SST anomaly reconstruction could be an artifact stemming from the selective dissolution of Mg-rich domains within the planktic foraminifer shells (e.g., Dekens et al., 2002; Rosenthal et al., 2000), which would attenuate the true amplitude of the local SST anomaly expressed in both of the Mg/Ca records. The drop in sedimentary calcite content associated with the CIE onset at Site 690 is a common feature of pelagic PETM sections (e.g., Bralower et al., 2014; Colosimo et al., 2006; Thomas et al., 1999) and reflects a pulse of intensified carbonate dissolution fueled by a $CO_2$-induced drop in ocean pH (Dickens et al., 1997; Penman et al., 2014; Zachos et al., 2005). Thus, a possible role for selective dissolution is consistent with the decrease in sedimentary calcite content and increase in planktic foraminifer shell fragmentation, as documented by Kelly et al. (2005), over the same interval featuring the Mg/Ca-based SST anomaly in the Site 690 PETM record. It is also possible that carbonate dissolution at Site 690 was more severe and that the basal stratigraphy of this PETM section may be incomplete as recently argued by others (Ajayi et al., 2020; Zhang et al., 2020). If the base of the CIE interval is truncated by hiatus, then the ~4–5°C of warming may represent a minimum.

This being said, we note that signs of intra-shell dissolution and etching were not observed in the many shells cross-sectioned for in situ analyses, although we acknowledge that, while the analyzed domains within the acarininid shells are better preserved than other parts of the same shells, they are likely not pristine. To a first approximation, secular variation in our Mg/Ca-based SST anomaly record appears to track model (LOSCAR) simulations for carbon input during the PETM (Zeebe et al., 2009). Specifically, the transient (<10 kyr) peak in SSTs reflects enhanced greenhouse radiative forcing caused by a large carbon-input event at the CIE onset followed by a more prolonged period (~50 kyr) of slightly cooler but still warm SSTs sustained by continued carbon release at slower rates over the main part of the CIE. Thus, the stratigraphic profile of our Mg/Ca-based SST anomaly curve may reflect secular variation in radiative forcing at this climatically sensitive location driven by two phases of carbon input that differ in their timing, duration, and emission rate during the PETM.

### 4.2. Changes in Surface Ocean $\delta^{18}O_{sw}$ and SSS at Site 690

The most parsimonious explanation for the disparities seen between the $\delta^{18}O_{SIMS}$ and Mg/Ca SST anomaly records is local changes in surface $\delta^{18}O_{sw}$ driven by secular variation in the precipitation-evaporation balance at Site 690. To explore the implications of this alternative interpretation, we used the $\Delta\delta^{18}O_{shell}/\Delta T$ relation of 0.213‰/°C to convert the differences between corresponding $\delta^{18}O_{SIMS}$ and Mg/Ca SSTs to expected changes in surface $\delta^{18}O_{sw}$ (Zachos et al., 2003). The resulting record reveals that a brief excursion to higher surface $\delta^{18}O_{sw}$ values coincided with peak PETM warming just after the CIE onset in the $\delta^{13}C_{acarininid}$ record (Figure 3b). However, the most salient feature is a prominent decrease, where surface $\delta^{18}O_{sw}$ values drop as low as −1.4‰ relative to the pre-CIE baseline over the interval (+30 to +80 ka) in which the $\delta^{18}O_{SIMS}$ minimum occurs. This finding differs from the long-held view that the $\delta^{18}O_{shell}$ minimum at +50 ka signals peak PETM warming (e.g., Kennett & Stott, 1991) and indicates that this $\delta^{18}O_{shell}$ minimum actually reflects a significant decrease in surface $\delta^{18}O_{sw}$ at Site 690. Surface $\delta^{18}O_{sw}$ values subsequently increase to values approaching the pre-CIE baseline at about +80 ka (Figure 3b).

Conversion of the surface $\delta^{18}O_{sw}$ values to SSS anomalies indicates that *peak* PETM warming was accompanied by a brief increase of ~2 ppt in SSS at Site 690 (Figure 3c). The width of the "salinity anomaly field" is a function of the selected $\Delta\delta^{18}O_{sw}/D_{salinity}$ relation, which varies from 0.25‰/salinity unit to 0.50‰/salinity unit (Zachos et al., 2003). On the basis of our paired $\delta^{18}O_{SIMS}$:Mg/Ca records, we conclude that peak PETM warming and an increase in SSS, reflecting a transient shift to warmer, more arid conditions at Site 690, was tightly coupled to initial carbon input. The ensuing $\delta^{18}O_{sw}$ minimum equates to a reduction in SSS beginning at about +30 ka with the lowest values (~2.9 to 5.8 ppt lower than pre-CIE baseline) occurring at about +50 ka (Figure 3c). This local negative SSS anomaly signals a transient increase in mean annual precipitation sustained by an increase in the poleward flux of atmospheric moisture at Site 690. Computed SSS anomalies subsequently increase to values approaching the pre-CIE baseline at about +80 ka (Figure 3c).

### 4.3. Implications for Carbon Cycling and Continental Weathering During the PETM

Such extreme fluctuations in the meridional balance between precipitation and evaporation would have influenced carbon cycling over the course of the PETM (John et al., 2008). If the initial shift to warmer, drier conditions occurred over geographically expansive tracts of the mid- and high-latitudes then the oxidation of sedimentary organic matter may have contributed to the $CO_2$ flux emitted during the early stages of the PETM (e.g., Kurtz et al., 2003; Panchuk et al., 2008). The ensuing reversal to slightly cooler SSTs, but substantially lower SSSs, is the most robust feature delineated by our paired $\delta^{18}O_{SIMS}$:Mg/Ca record and culminates in a negative SSS anomaly that is ~4 ppt lower than the mean pre-CIE value (Figure 3c). This significant downturn in SSS signals a major change in the meridional balance between precipitation and evaporation, which in turn increased the poleward transport of atmospheric moisture and mean annual precipitation at Site 690. This particular result is consonant with General Circulation Models predicting greater poleward migration of storm tracks under a warmer climate regime (Caballero & Langen, 2005). Such an extreme turnabout in hydrological regime would have altered spatial patterns of continental erosion/sedimentation and likely intensified chemical weathering of landmasses (Carmichael et al., 2017, 2018). Such a supposition is supported by the marked increases in siliciclastic sedimentation at nearshore, shallow marine sites during the PETM (John et al., 2008; Nicolo et al., 2010), and by a concomitant change in clay mineralogy to predominantly kaolinite in some geological sections (Bolle &

Adatte, 2001; Clechenko et al., 2007; Gibson et al., 2000). Although the syngenecity of kaolinitization and PETM conditions has been questioned (John et al., 2012; Thiry, 2000), and even attributed to the redeposition of a rapidly weathered impact ejecta dust blanket (Kent et al., 2003), a similar increase in kaolinite amongst detrital clay assemblages in the Site 690 section has been ascribed to increased continental weathering and freshwater input driven by a transient increase in atmospheric heat transport toward the poles (Kelly et al., 2005; Robert & Kennett, 1994). Here, we note that the latter interpretation (Robert & Kennett, 1994) is consistent with the prominent negative SSS anomaly recorded over the CIE interval (+30 ka to +80 ka) at Site 690. The apparent lag in local hydrologic response to warming might be related to orbital effects (Kiehl et al., 2018).

## 5. Conclusions

Paired $\delta^{18}$O:Mg/Ca analyses, acquired in situ from micrometer-scale domains within shells of the planktic foraminifer, *A. soldadoensis*, indicate that peak PETM warming was coupled to an increase in SSS at ODP Site 690 (Weddell Sea). This initial shift to hotter, more arid conditions was tightly coupled to the initial release of massive quantities of carbon to the atmosphere. The local SST anomaly of ~4°C reflecting peak PETM warming at Site 690 may represent a minimum owing to the possibility that the base of the PETM section is truncated by a hiatus. A prominent ~4 ppt decrease in SSS, back-calculated from paired $\delta^{18}$O:Mg/Ca measurements, is observed ~50 ka after peak PETM warming. This negative SSS ($\delta^{18}O_{sw}$) anomaly coincides with a minimum in the Site 690 planktic foraminifer $\delta^{18}$O record that has previously been cited as evidence for polar amplification of PETM warmth in the absence of ice-albedo effects. Thus, our revised interpretation posits that this $\delta^{18}$O minimum actually signals a decrease in surface-ocean $\delta^{18}O_{sw}$ fostered by a transient increase in mean annual precipitation in the Weddell Sea region, thereby corroborating the view that the poleward flux of atmospheric moisture temporarily increased during a distinctive stage of the PETM.

Such data-based reconstructions of the response of Earth's hydrological cycle to greenhouse gas forcing are vital to understanding how atmospheric moisture and latent heat were redistributed across the planet during past episodes of global warming. This study confirms that Earth's hydrological cycle was profoundly perturbed by massive carbon input during the PETM, and the highly resolved chronostratigraphy of the Site 690 section provides temporal constraints on secular variation in the poleward flux of atmospheric moisture and latent heat. The surface $\delta^{18}O_{sw}$ (and SSS) record herein reconstructed for the Site 690 PETM section improves geographic coverage in the climatically sensitive circum-Antarctic region, which should prove useful for testing outcomes of computational models designed to simulate PETM climatic conditions (e.g., Zhu et al., 2020).

## Data Availability Statement

Data tables of in situ $\delta^{18}$O and Mg/Ca analyses are available from the PANGAEA domain repository (https://doi.pangaea.de/10.1594/PANGAEA.914650, https://doi.pangaea.de/10.1594/PANGAEA.914651).

**Acknowledgments**

This research was supported by NSF OCE-1131516 and the Wisconsin Alumni Research Foundation to D.C.K. This research used samples provided by the International Ocean Discovery Program (IODP). WiscSIMS is supported by NSF EAR-1658823 and the University of Wisconsin-Madison. Sample mounts were prepared by Brian Hess.

## References

Ajayi, S., Kump, L. R., Ridgwell, A., Kirtland Turner, S., Hay, C. C., & Bralower, T. J. (2020). Evaluation of Paleocene-Eocene thermal maximum carbon isotope record completeness—An illustration of the potential of dynamic time warping in aligning paleo-proxy records. *Geochemistry, Geophysics, Geosystems*, *21*, e2019GC008620. https://doi.org/10.1029/2019GC008620

Anand, P., Elderfield, H., & Conte, M. H. (2003). Calibration of Mg/Ca thermometry in planktonic foraminifera from a sediment trap time series. *Paleoceanography*, *18*(2), 1050. https://doi.org/10.1029/2002PA000846

Anand, P., Kroon, D., Singh, A. D., Ganeshram, R. S., Ganssen, G., & Elderfield, H. (2008). Coupled sea surface temperature–seawater $\delta^{18}$O reconstructions in the Arabian Sea at the millennial scale for the last 35 ka. *Paleoceanography*, *23*(4), PA4207. https://doi.org/10.1029/2007PA001564

Aze, T., Pearson, P. N., Dickson, A. J., Badger, M. P. S., Bown, P. R., Pancost, R. D., et al. (2014). Extreme warming of tropical waters during the Paleocene–Eocene thermal maximum. *Geology*, *42*(9). https://doi.org/10.1130/g35637.1

Babila, T. L., Penman, D. E., Hönisch, B., Kelly, D. C., Bralower, T. J., Rosenthal, Y., & Zachos, J. C. (2018). Capturing the global signature of surface ocean acidification during the Palaeocene–Eocene thermal maximum. *Philosophical Transactions of the Royal Society A: Mathematical, Physical and Engineering Sciences*, *376*(2130), 20,170,072. https://doi.org/10.1098/rsta.2017.0072

Babila, T. L., Rosenthal, Y., Wright, J. D., & Miller, K. G. (2016). A continental shelf perspective of ocean acidification and temperature evolution during the Paleocene-Eocene thermal maximum. *Geology*, *44*(4), 275–278. https://doi.org/10.1130/g37522.1

Bains, S., Corfield, R. M., & Norris, R. D. (1999). Mechanisms of climate warming at the end of the Paleocene. *Science*, *285*(5428), 724–727. https://doi.org/10.1126/science.285.5428.724

Barker, P. F., Kennett, J. P., & (1988). 6. Site 690. Shipboard scientific party. In P. F. Barker, & J. P. Kennett (Eds.), *Proceedings of the Ocean Drilling Program, Scientific Results* (Vol. 113, pp. 183–292). Texas: College Station.

Bemis, B. E., Spero, H. J., Bijma, J., & Lea, D. W. (1998). Reevaluation of the oxygen isotopic composition of planktonic foraminifera: Experimental results and revised paleotemperature equations. *Paleoceanography*, *13*(2), 150–160. https://doi.org/10.1029/98PA00070

Bentov, S., & Erez, J. (2006). Impact of biomineralization processes on the Mg content of foraminiferal shells: A biological perspective. *Geochemistry, Geophysics, Geosystems*, *7*, Q01P08. https://doi.org/10.1029/2005GC001015

Blow, W. H. (1979). *The Cainozoic Globigerinida*. Leiden, The Netherlands: E.J. Brill.

Bolle, M. P., & Adatte, T. (2001). Palaeocene-early Eocene climatic evolution in the Tethyan realm: Clay mineral evidence. *Clay Minerals*, *36*(2), 249–261. https://doi.org/10.1180/000985501750177979

Bowen, G. J., Beerling, D. J., Koch, P. L., Zachos, J. C., & Quattlebaum, T. (2004). A humid climate state during the Palaeocene/Eocene thermal maximum. *Nature*, *432*(7016), 495–499. https://doi.org/10.1038/nature03115

Boyle, E. A., & Keigwin, L. D. (1985). Comparison of Atlantic and Pacific paleochemical records for the last 215.000 years: Changes in deep ocean circulation and chemical inventories. *Earth and Planetary Science Letters*, *76*, 135–150. https://doi.org/10.1016/0012-821x(85)90154-2

Bralower, T. J. (2002). Evidence of surface water oligotrophy during the Paleocene-Eocene thermal maximum: Nannofossil assemblage data from ocean drilling program Site 690, Maud rise, Weddell Sea. *Paleoceanography*, *17*(2), 1023. https://doi.org/10.1029/2001PA000662

Bralower, T. J., Meissner, K. J., Alexander, K., & Thomas, D. J. (2014). The dynamics of global change at the Paleocene-Eocene thermal maximum: A data-model comparison. *Geochemistry, Geophysics, Geosystems*, *15*(10), 3830–3848. https://doi.org/10.1002/2014GC005474

Brown, R. E., Anderson, L. D., Thomas, E., & Zachos, J. C. (2011). A core-top calibration of B/Ca in the benthic foraminifers Nuttallides umbonifera and Oridorsalis umbonatus: A proxy for Cenozoic bottom water carbonate saturation. *Earth and Planetary Science Letters*, *310*(3–4), 360–368. https://doi.org/10.1016/j.epsl.2011.08.023

Caballero, R., & Langen, P. L. (2005). The dynamic range of poleward energy transport in an atmospheric general circulation model. *Geophysical Research Letters*, *32*, L02705. https://doi.org/10.1029/2004GL021581

Carmichael, M. J., Inglis, G. N., Badger, M. P., Naafs, B. D. A., Behrooz, L., Remmelzwaal, S., et al. (2017). Hydrological and associated biogeochemical consequences of rapid global warming during the Paleocene-Eocene thermal maximum. *Global and Planetary Change*, *157*, 114–138. https://doi.org/10.1016/j.gloplacha.2017.07.014

Carmichael, M. J., Pancost, R. D., & Lunt, D. J. (2018). Changes in the occurrence of extreme precipitation events at the Paleocene–Eocene thermal maximum. *Earth and Planetary Science Letters*, *501*, 24–36. https://doi.org/10.1016/j.epsl.2018.08.005

Cavosie, A. J., Valley, J. W., Wilde, S. A., & E.I.M.F (2005). Magmatic $\delta^{18}O$ in 4400–3900 ma detrital zircons: A record of the alteration and recycling of crust in the early Archean. *Earth and Planetary Science Letters*, *235*(3–4), 663–681. https://doi.org/10.1016/j.epsl.2005.04.028

Clechenko, E. R., Kelly, D. C., Harrington, G. J., & Stiles, C. A. (2007). Terrestrial records of a regional weathering profile at the Paleocene-Eocene boundary in the Williston Basin of North Dakota. *Geological Society of America Bulletin*, *119*(3–4), 428–442. https://doi.org/10.1130/b26010.1

Clementz, M. T., & Sewall, J. O. (2011). Latitudinal gradients in greenhouse seawater $\delta^{18}O$: Evidence from Eocene Sirenian tooth enamel. *Science*, *332*(6028), 455–458. https://doi.org/10.1126/science.1201182

Coggon, R. M., Teagle, D. A. H., Smith-Duque, C. E., Alt, J. C., & Cooper, M. J. (2010). Reconstructing past seawater Mg/Ca and Sr/Ca from Mid-Ocean ridge flank calcium carbonate veins. *Science*, *327*(5969), 1114–1117. https://doi.org/10.1126/science.1182252

Colosimo, A., Bralower, T. J., & Zachos, J. C. (2006). Evidence for lysocline shoaling at the Paleocene/Eocene thermal maximum on Shatsky rise, Northwest Pacific. In T. J. Bralower, I. P. Silva, & M. J. Malone (Eds.), *Proceedings of the Ocean Drilling Program, Scientific Results* (Vol. 198, pp. 1–36). TX: College Station.

Craig, H., & Gordon, L. I. (1965). Deuterium and oxygen 18 variations in the ocean and the marine atmosphere. E. Tongiorgi (Ed.), *Stable Isotopes in oceanographic studies and paleotemperatures* (pp. 9–130). Spoleto, Italy: Consiglio Nazionale Delle Ricerche Laboratorio Di Geologia Nucleare - Pisa.

Dahl, K. A., & Oppo, D. W. (2006). Sea surface temperature pattern reconstructions in the Arabian Sea. *Paleoceanography*, *21*, PA1014. https://doi.org/10.1029/2005PA001162

DeConto, R. M., Galeotti, S., Pagani, M., Tracy, D., Schaefer, K., Zhang, T., et al. (2012). Past extreme warming events linked to massive carbon release from thawing permafrost. *Nature*, *484*(7392), 87–91. https://doi.org/10.1038/nature10929

Dekens, P. S., Lea, D. W., Pak, D. K., & Spero, H. J. (2002). Core top calibration of Mg/Ca in tropical foraminifera: Refining paleotemperature estimation. *Geochemistry, Geophysics, Geosystems*, *3*(4), 1022. https://doi.org/10.1029/2001GC000200

Dickens, G. R., Castillo, M. M., & Walker, J. C. G. (1997). A blast of gas in the latest Paleocene: Simulating first-order effects of massive dissociation of oceanic methane hydrate. *Geology*, *25*(3), 259–262. https://doi.org/10.1130/0091-7613(1997)025<0259:abogit>2.3.co;2

Dickens, G. R., O'Neil, J. R., Rea, D. K., & Owen, M. (1995). Dissociation of oceanic methane hydrate as a cause of the carbon isotope excursion at the end of the Paleocene. *Paleoceanography*, *10*, 965–971. https://doi.org/10.1029/95pa02087

Egger, H., Fenner, J., Heilmann-Clausen, C., Rögl, F., Sachsenhofer, R. F., & Schmitz, B. (2003). Paleoproductivity of the northwestern Tethyan margin (Anthering section, Austria) across the Paleocene-Eocene transition. In S. L. Wing, P. D. Gingerich, B. Schmitz, & E. Thomas (Eds.), *Climates in the Early Paleogene* (pp. 133–146). Boulder, Colorado: Geological Society of America Special Paper.

Eggins, S. M., De Decker, P., & Marshall, J. (2003). Mg/Ca variations in planktonic foraminifera tests: Implications for reconstructing paleo-seawater temperature and habitat migration. *Earth and Planetary Science Letters*, *212*, 291–306. https://doi.org/10.1016/s0012-821x(03)00283-8

Elderfield, H., & Ganssen, G. (2000). Past temperature and δ18O of surface ocean waters inferred from foraminiferal Mg/Ca ratios. *Nature*, *405*(6785), 442–445. https://doi.org/10.1038/35013033

Emiliani, C. (1955). Pleistocene temperatures. *Journal of Geology*, *63*, 537–578. https://doi.org/10.1086/626295

Evans, D., Brierley, C., Raymo, M. E., Erez, J., & Müller, W. (2016). Planktic foraminifera shell chemistry response to seawater chemistry: Pliocene–Pleistocene seawater Mg/Ca, temperature and sea level change. *Earth and Planetary Science Letters*, *438*, 139–148. https://doi.org/10.1016/j.epsl.2016.01.013

Evans, D., Erez, J., Oron, S., & Müller, W. (2015). Mg/Ca-temperature and seawater-test chemistry relationships in the shallow-dwelling large benthic foraminifera Operculina ammonoides. *Geochimica et Cosmochimica Acta*, *148*(0), 325–342. https://doi.org/10.1016/j.gca.2014.09.039

Evans, D., Sagoo, N., Renema, W., Cotton, L. J., Müller, W., Todd, J. A., et al. (2018). Eocene greenhouse climate revealed by coupled clumped isotope-Mg/Ca thermometry. *Proceedings of the National Academy of Sciences*, *115*(6), 1174–1179. https://doi.org/10.1073/pnas.1714744115

Evans, D., Wade, B. S., Henehan, M., Erez, J., & Müller, W. (2015). Revisiting carbonate chemistry controls on planktic foraminifera Mg/Ca: Implications for sea surface temperature and hydrology shifts over the Paleocene–Eocene thermal maximum and Eocene–Oligocene transition. *Climate of the Past Discussions*, *11*(4), 3143–3185. https://doi.org/10.5194/cpd-11-3143-2015

Evans, D., Wade, B. S., Henehan, M., Erez, J., & Müller, W. (2016). Revisiting carbonate chemistry controls on planktic foraminifera Mg/Ca: Implications for sea surface temperature and hydrology shifts over the Paleocene–Eocene thermal maximum and Eocene–Oligocene transition. *Climate of the Past*, *12*(4), 819–835. https://doi.org/10.5194/cp-12-819-2016

Farley, K. A., & Eltgroth, S. F. (2003). An alternative age model for the Paleocene–Eocene thermal maximum using extraterrestrial 3He. *Earth and Planetary Science Letters*, *208*(3–4), 135–148. https://doi.org/10.1016/s0012-821x(03)00017-7

Flower, B. P., Hastings, D. W., Hill, H. W., & Quinn, T. M. (2004). Phasing of deglacial warming and Laurentide ice sheet meltwater in the Gulf of Mexico. *Geology*, *32*(7), 597–600. https://doi.org/10.1130/g20604.1

Foreman, B. Z., Heller, P. L., & Clementz, M. T. (2012). Fluvial response to abrupt global warming at the Palaeocene/Eocene boundary. *Nature*, *491*(7422), 92–95. https://doi.org/10.1038/nature11513

Francis, J. E. (1988). A 50-million-year-old fossil Forest from Strathcona fiord, Ellesmere Island, Arctic Canada: Evidence for a warm polar climate. *Arctic*, *4*(4), 314–318. https://doi.org/10.14430/arctic1738

Frieling, J., Gebhardt, H., Huber, M., Adekeye, O. A., Akande, S. O., Reichart, G.-J., et al. (2017). Extreme warmth and heat-stressed plankton in the tropics during the Paleocene-Eocene thermal maximum. *Science Advances*, *3*(3), e1600891. https://doi.org/10.1126/sciadv.1600891

Gibson, T. G., Bybell, L. M., & Mason, D. B. (2000). Stratigraphic and climatic implications of clay mineral changes around the Paleocene/Eocene boundary of the northeastern US margin. *Sedimentary Geology*, *134*(1–2), 65–92. https://doi.org/10.1016/s0037-0738(00)00014-2

Gray, W. R., Weldeab, S., Lea, D. W., Rosenthal, Y., Gruber, N., Donner, B., & Fischer, G. (2018). The effects of temperature, salinity, and the carbonate system on Mg/Ca in Globigerinoides ruber (white): A global sediment trap calibration. *Earth and Planetary Science Letters*, *482*, 607–620. https://doi.org/10.1016/j.epsl.2017.11.026

Gutjahr, M., Ridgwell, A., Sexton, P. F., Anagnostou, E., Pearson, P. N., Pälike, H., et al. (2017). Very large release of mostly volcanic carbon during the Palaeocene-Eocene thermal maximum. *Nature*, *548*(7669), 573–577. https://doi.org/10.1038/nature23646

Handley, L., O'Halloran, A., Pearson, P. N., Hawkins, E., Nicholas, C. J., Schouten, S., et al. (2012). Changes in the hydrological cycle in tropical East Africa during the Paleocene–Eocene Thermal Maximum. *Palaeogeography, Palaeoclimatology, Palaeoecology*, *329–330*(0), 10–21. https://doi.org/10.1016/j.palaeo.2012.02.002

Hay, W. W., DeConto, R. M., Wold, C. N., Wilson, K. M., Voigt, S., Schulz, M., et al. (1999). *Alternative global cretaceous paleogeography* (Vol. *332*, pp. 1–47). Boulder, Colorado: Geological Society of America Special Papers.

Held, I. M., & Soden, B. J. (2000). Water Vapor Feedback and Global Warming. *Annual Review of Energy and the Environment*, *25*(1), 441–475. https://doi.org/10.1146/annurev.energy.25.1.441

Held, I. M., & Soden, B. J. (2006). Robust responses of the hydrological cycle to global warming. *Journal of Climate*, *19*(21), 5686–5699. https://doi.org/10.1175/jcli3990.1

Higgins, J. A., & Schrag, D. P. (2006). Beyond methane: Towards a theory for the Paleocene–Eocene thermal maximum. *Earth and Planetary Science Letters*, *245*(3–4), 523–537. https://doi.org/10.1016/j.epsl.2006.03.009

Hönisch, B., Allen, K. A., Lea, D. W., Spero, H. J., Eggins, S. M., Arbuszewski, J., et al. (2013). The influence of salinity on Mg/Ca in planktic foraminifers—Evidence from cultures, core-top sediments and complementary δ18O. *Geochimica et Cosmochimica Acta*, *121*(0), 196–213. https://doi.org/10.1016/j.gca.2013.07.028

Huber, M., & Goldner, A. (2012). Eocene monsoons. *Journal of Asian Earth Sciences*, *44*(0), 3–23. https://doi.org/10.1016/j.jseaes.2011.09.014

Hupp, B. N., Kelly, D. C., Zachos, J. C., & Bralower, T. J. (2019). Effects of size-dependent sediment mixing on deep-sea records of the Paleocene-Eocene thermal maximum. *Geology*, *47*(8), 749–752. https://doi.org/10.1130/g46042.1

John, C. M., Banerjee, N. R., Longstaffe, F. J., Sica, C., Law, K. R., & Zachos, J. C. (2012). Clay assemblage and oxygen isotopic constraints on the weathering response to the Paleocene-Eocene thermal maximum, east coast of North America. *Geology*, *40*(7), 591–594. https://doi.org/10.1130/g32785.1

John, C. M., Bohaty, S. M., Zachos, J. C., Sluijs, A., Gibbs, S., Brinkhuis, H., & Bralower, T. J. (2008). North American continental margin records of the Paleocene-Eocene thermal maximum: Implications for global carbon and hydrological cycling. *Paleoceanography*, *23*, PA2217. https://doi.org/10.1029/2007pa001465

Jones, T. D., Lunt, D. J., Schmidt, D. N., Ridgwell, A., Sluijs, A., Valdes, P. J., & Maslin, M. (2013). Climate model and proxy data constraints on ocean warming across the Paleocene–Eocene thermal maximum. *Earth Science Reviews*, *125*, 123–145. https://doi.org/10.1016/j.earscirev.2013.07.004

Kelly, D. C. (2002). Response of Antarctic (ODP Site 690) planktonic foraminifera to the Paleocene–Eocene thermal maximum: Faunal evidence for ocean/climate change. *Paleoceanography*, *17*(4), 1071. https://doi.org/10.1029/2002PA000761

Kelly, D. C., Zachos, J. C., Bralower, T. J., & Schellenberg, S. A. (2005). Enhanced terrestrial weathering/runoff and surface ocean carbonate production during the recovery stages of the Paleocene-Eocene thermal maximum. *Paleoceanography*, *20*, PA4023. https://doi.org/10.1029/2005PA001163

Kennett, J. P., & Stott, L. D. (1991). Abrupt deep-sea warming, palaeoceanographic changes and benthic extinctions at the end of the Paleocene. *Nature*, *353*, 225–229. https://doi.org/10.1038/353225a0

Kent, D. V., Cramer, B. S., Lanci, L., Wang, D., Wright, J. D., & Van der Voo, R. (2003). A case for a comet impact trigger for the Paleocene/Eocene thermal maximum and carbon isotope excursion. *Earth and Planetary Science Letters*, *211*(1–2), 13–26. https://doi.org/10.1016/S0012-821X(03)00188-2.

Kiehl, J. T., Shields, C. A., Snyder, M. A., Zachos, J. C., & Rothstein, M. (2018). Greenhouse-and orbital-forced climate extremes during the early Eocene. *Philosophical Transactions of the Royal Society A: Mathematical, Physical and Engineering Sciences*, *376*(2130), 20,170,085. https://doi.org/10.1098/rsta.2017.0085

Killingley, J. S. (1983). Effects of diagenetic recrystallization on $^{18}O/^{16}O$ values of deep-sea sediments. *Nature*, *301*, 594–597. https://doi.org/10.1038/301594a0

Kirtland Turner, S., Hull, P. M., Kump, L. R., & Ridgwell, A. (2017). A probabilistic assessment of the rapidity of PETM onset. *Nature Communications*, *8*. https://doi.org/10.1038/s41467-017-00292-2

Kita, N. T., Ushikubo, T., Fu, B., & Valley, J. W. (2009). High precision SIMS oxygen isotope analysis and the effect of sample topography. *Chemical Geology*, *264*(1–4), 43–57. https://doi.org/10.1016/j.chemgeo.2009.02.012

Kozdon, R., Kelly, D. C., Kita, N. T., Fournelle, J. H., & Valley, J. W. (2011). Planktonic foraminiferal oxygen isotope analysis by ion microprobe technique suggests warm tropical sea surface temperatures during the early Paleogene. *Paleoceanography*, *26*(3), PA3206. https://doi.org/10.1029/2010PA002056

Kozdon, R., Kelly, D. C., Kitajima, K., Strickland, A., Fournelle, J. H., & Valley, J. W. (2013). In situ δ18O and Mg/Ca analyses of diagenetic and planktic foraminiferal calcite preserved in a deep-sea record of the Paleocene-Eocene thermal maximum. *Paleoceanography*, *28*, 517–528. https://doi.org/10.1002/palo.20048

Kozdon, R., Ushikubo, T., Kita, N. T., Spicuzza, M., & Valley, J. W. (2009). Intratest oxygen isotope variability in the planktonic foraminifer *N. pachyderma:* Real vs. apparent vital effects by ion microprobe. *Chemical Geology*, *258*, 327–337. https://doi.org/10.1016/j.chemgeo.2008.10.032

Kraus, M. J., & Riggins, S. (2007). Transient drying during the Paleocene–Eocene Thermal Maximum (PETM): Analysis of paleosols in the bighorn basin, Wyoming. *Palaeogeography, Palaeoclimatology, Palaeoecology*, *245*(3–4), 444–461. https://doi.org/10.1016/j.palaeo.2006.09.011

Kurtz, A. C., Kump, L. R., Arthur, M. A., Zachos, J. C., & Paytan, A. (2003). Early Cenozoic decoupling of the global carbon and sulfur cycles. *Paleoceanography*, *18*(4), 1090. https://doi.org/10.1029/2003PA000908

Larrasoaña, J. C., Roberts, A. P., Chang, L., Schellenberg, S. A., Fitz Gerald, J. D., Norris, R. D., & Zachos, J. C. (2012). Magnetotactic bacterial response to Antarctic dust supply during the Palaeocene–Eocene thermal maximum. *Earth and Planetary Science Letters*, *333–334*, 122–133. https://doi.org/10.1016/j.epsl.2012.04.003

Lea, D. W., Mashiotta, T. A., & Spero, H. J. (1999). Controls on magnesium and strontium uptake in planktonic foraminifera determined by live culturing. *Geochimica et Cosmochimica Acta*, *63*(16), 2369–2379. https://doi.org/10.1016/s0016-7037(99)00197-0

Martin, P. A., & Lea, D. W. (2002). A simple evaluation of cleaning procedures on fossil benthic foraminiferal Mg/Ca. *Geochemistry, Geophysics, Geosystems*, *3*(10), 8401. https://doi.org/10.1029/2001GC000280

McInerney, F. A., & Wing, S. L. (2011). The Paleocene-Eocene thermal maximum: A perturbation of carbon cycle, climate, and biosphere with implications for the future. *Annual Review of Earth and Planetary Sciences*, *39*(1), 489–516. https://doi.org/10.1146/annurev-earth-040610-133431

Nicolo, M. J., Dickens, G. R., & Hollis, C. J. (2010). South Pacific intermediate water oxygen depletion at the onset of the Paleocene-Eocene thermal maximum as depicted in New Zealand margin sections. *Paleoceanography*, *25*, PA4210. https://doi.org/10.1029/2009PA001904

Nuernberg, D. (1995). Magnesium in tests of Neogloboquadrina pachyderma sinistral from high northern and southern latitudes. *The Journal of Foraminiferal Research*, *25*, (4), 350–368. http://doi.org/10.2113/gsjfr.25.4.350

Pagani, M., Huber, M., & Sageman, B. B. (2013). Greenhouse climates. In *Treatise on Geochemistry: Second Edition* (pp. 281–304). Oxford, England: Elsevier Inc.

Pagani, M., Pedentchouk, N., Huber, M., Sluijs, A., Schouten, S., Brinkhuis, H., et al. (2006). Arctic hydrology during global warming at the Palaeocene/Eocene thermal maximum. *Nature*, *442*(7103), 671–675. https://doi.org/10.1038/nature05043

Panchuk, K., Ridgwell, A., & Kump, L. R. (2008). Sedimentary response to Paleocene-Eocene Thermal Maximum carbon release: A model-data comparison. *Geology*, *36*(4), 315–318. https://doi.org/10.1130/g24474a.1

Pearson, P. N., Ditchfield, P. W., Singano, J., Harcourt-Brown, K. G., Nicholas, C. J., Olsson, R. K., et al. (2001). Warm tropical sea surface temperatures in the late cretaceous and Eocene epochs. *Nature*, *413*(6855), 481–487. https://doi.org/10.1038/35097000

Penman, D. E., Hönisch, B., Zeebe, R. E., Thomas, E., & Zachos, J. C. (2014). Rapid and sustained surface ocean acidification during the Paleocene-Eocene Thermal Maximum. *Paleoceanography*, *29*, 357–369. https://doi.org/10.1002/2014PA002621

Pierrehumbert, R. T. (2002). The hydrologic cycle in deep-time climate problems. *Nature*, *419*(6903), 191–198. https://doi.org/10.1038/nature01088

Pujalte, V., Monechi, S., Ortíz, S., Orue-Etxebarria, X., Rodríguez-Tovar, F., & Schmitz, B. (2019). Microcodium-rich turbidites in hemipelagic sediments during the Paleocene–Eocene thermal maximum: Evidence for extreme precipitation events in a Mediterranean climate (Río Gor section, southern Spain). *Global and Planetary Change*, *178*, 153–167. https://doi.org/10.1016/j.gloplacha.2019.04.018

Quillévéré, F., Norris, R. D., Moussa, I., & Berggren, W. A. (2001). Role of photosymbiosis and biogeography in the diversification of early Paleogene acarininids (planktonic foraminifera). *Paleobiology*, *27*, 311–326. https://doi.org/10.1666/0094-8373(2001)027<0311:ropabi>2.0.co;2

Robert, C., & Kennett, J. P. (1994). Antarctic subtropical humid episode at the Paleocene-Eocene boundary: Clay-mineral evidence. *Geology*, *22*(3), 211–214. https://doi.org/10.1130/0091-7613(1994)022<0211:asheat>2.3.co;2

Röhl, U., Bralower, T. J., Norris, R. D., & Wefer, G. (2000). New chronology for the late Paleocene thermal maximum and its environmental implications. *Geology*, *28*, 927–930. https://doi.org/10.1130/0091-7613(2000)28<927:ncftlp>2.0.co;2

Röhl, U., Westerhold, T., Bralower, T. J., & Zachos, J. C. (2007). On the duration of the Paleocene-Eocene thermal maximum (PETM). *Geochemistry, Geophysics, Geosystems*, *8*, Q12002. https://doi.org/10.1029/2007GC001784

Rosenthal, Y., Boyle, E. A., & Slowey, N. (1997). Temperature control on the incorporation of magnesium, strontium, fluorine, and cadmium into benthic foraminiferal shells from Little Bahama Bank: Prospects for thermocline paleoceanography. *Geochimica et Cosmochimica Acta*, *61*(17), 3633–3643. https://doi.org/10.1016/S0016-7037(97)00181-6

Rosenthal, Y., Lohmann, G. P., Lohmann, K. C., & Sherrell, R. M. (2000). Incorporation and preservation of mg in Globigerinoides sacculifer: Implications for reconstructing the temperature and 18O/16O of seawater. *Paleoceanography*, *15*(1), 135–145. https://doi.org/10.1029/1999PA000415

Schmitt, R. W. (1995). The ocean component of the global water cycle. *Reviews of Geophysics*, *33*(S2), 1395–1409. https://doi.org/10.1029/95RG00184

Schmitz, B., & Pujalte, V. (2007). Abrupt increase in seasonal extreme precipitation at the Paleocene-Eocene boundary. *Geology*, *35*(3), 215–218. https://doi.org/10.1130/g23261a.1

Segev, E., & Erez, J. (2006). Effect of Mg/Ca ratio in seawater on shell composition in shallow benthic foraminifera. *Geochemistry, Geophysics, Geosystems*, *7*, Q02P09. https://doi.org/10.1029/2005GC000969

Sexton, P. F., Wilson, P. A., & Pearson, P. N. (2006). Microstructural and geochemical perspectives on planktic foraminiferal preservation: "glassy" versus "frosty". *Geochemistry, Geophysics, Geosystems*, *7*, Q12P19. https://doi.org/10.1029/2006GC001291

Shackleton, N. (1967). Oxygen isotope analyses and Pleistocene temperatures re-assessed. *Nature*, *215*(5096), 15–17. https://doi.org/10.1038/215015a0

Shackleton, N. J. (1974). *Attainment of isotopic equilibrium between ocean water and the benthonic foraminifera genus Uvigerina*: Isotopic changes in the ocean during the last glacial, (Vol. 219, pp. 203–209). Paris, France: Colloques Internationaux du C.N.R.S.

Shackleton, N. J., & Kennett, J. P. (1975). Paleotemperature history of the Cenozoic and the initiation of Antarctic glaciation; oxygen and carbon isotope analyses in DSDP Sotes 277, 279, and 281. In J. P. Kennett, & R. E. Houtz (Eds.), *Initial Reports of the Deep Sea Drilling Project*, (pp. 743–755). Washington DC: U.S. government printing office.

Sluijs, A., Bijl, P. K., Schouten, S., Röhl, U., Reichart, G. J., & Brinkhuis, H. (2011). Southern Ocean warming, sea level and hydrological change during the Paleocene-Eocene thermal maximum. *Climate of the Past*, *7*(1), 47–61. https://doi.org/10.5194/cp-7-47-2011

Sluijs, A., Röhl, U., Schouten, S., Brumsack, H.-J., Sangiorgi, F., Sinninghe Damsté, J. S., & Brinkhuis, H. (2008). Arctic late Paleocene - early Eocene paleoenvironments with special emphasis on the Paleocene-Eocene thermal maximum (Lomonosov Ridge, Integrated Ocean Drilling Program Expedition 302). *Paleoceanography*, *23*(1), PA1S11. https://doi.org/10.1029/2007pa001495

Sluijs, A., Schouten, S., Pagani, M., Woltering, M., Brinkhuis, H., Sinninghe Damsté, J. S., et al. (2006). Subtropical Arctic Ocean temperatures during the Palaeocene/Eocene thermal maximum. *Nature*, *441*(7093), 610–613. https://doi.org/10.1038/nature04668

Spero, H. J., Bijma, J., Lea, D. W., & Bemis, B. E. (1997). Effect of seawater carbonate concentration on foraminiferal carbon and oxygen isotopes. *Nature*, *390*(6659), 497–500. https://doi.org/10.1038/37333

Svensen, H., Planke, S., Malthe-Sorenssen, A., Jamtveit, B., Myklebust, R., Rasmussen Eidem, T., & Rey, S. S. (2004). Release of methane from a volcanic basin as a mechanism for initial Eocene global warming. *Nature*, *429*(6991), 542–545. https://doi.org/10.1038/nature02566

Thiry, M. (2000). Palaeoclimatic interpretation of clay minerals in marine deposits: An outlook from the continental origin. *Earth Science Reviews*, *49*, 201–221. https://doi.org/10.1016/s0012-8252(99)00054-9

Thomas, D. J., Bralower, T. J., & Zachos, J. C. (1999). New evidence for subtropical warming during the late Paleocene thermal maximum: Stable isotopes from Deep Sea drilling project Site 527, Walvis ridge. *Paleoceanography*, *14*(5), 561–570. https://doi.org/10.1029/1999PA900031

Thomas, D. J., Zachos, J. C., Bralower, T. J., Thomas, E., & Bohaty, S. (2002). Warming the fuel for the fire: Evidence for the thermal dissociation of methane hydrate during the Paleocene-Eocene thermal maximum. *Geology*, *30*, 1067–1070. https://doi.org/10.1130/0091-7613(2002)030<1067:wtfftf>2.0.co;2

Thomas, E. (1990). Late cretaceous through Neogene deep-sea benthic foraminifers (Maud rise, Weddell Sea, Antarctica). In *Proceedings of the Ocean Drilling Program, Scientific Results* (Vol. 113, pp. 571–594). College Station, Texas, USA: Ocean Drilling Program.

Tipple, B. J., Pagani, M., Krishnan, S., Dirghangi, S. S., Galeotti, S., Agnini, C., et al. (2011). Coupled high-resolution marine and terrestrial records of carbon and hydrologic cycles variations during the Paleocene–Eocene thermal maximum (PETM). *Earth and Planetary Science Letters*, *311*(1–2), 82–92. https://doi.org/10.1016/j.epsl.2011.08.045

Uchikawa, J., & Zeebe, R. E. (2010). Examining possible effects of seawater pH decline on foraminiferal stable isotopes during the Paleocene-Eocene thermal maximum. *Paleoceanography*, *25*(2), PA2216. https://doi.org/10.1029/2009pa001864

Valley, J. W., & Kita, N. T. (2009). In situ oxygen isotope geochemistry by ion microprobe. In M. Fayek (Ed.), *MAC Short Course: Secondary Ion Mass Spectrometry in the Earth Sciences* (Vol. 41, pp. 16–63). Toronto, Ontario: Mineralogical Association of Canada.

Wing, S. L., Harrington, G. J., Smith, F. A., Bloch, J. I., Boyer, D. M., & Freeman, K. H. (2005). Transient floral change and rapid global warming at the Paleocene-Eocene boundary. *Science*, *310*(5750), 993–996. https://doi.org/10.1126/science.1116913

Wycech, J. B., Kelly, D. C., Kozdon, R., Orland, I. J., Spero, H. J., & Valley, J. W. (2018). Comparison of δ18O analyses on individual planktic foraminifer (Orbulina universa) shells by SIMS and gas-source mass spectrometry. *Chemical Geology*, *483*, 119–130. http://doi.org/10.1016/j.chemgeo.2018.02.028

Zachos, J. C., Dickens, G. R., & Zeebe, R. E. (2008). An early Cenozoic perspective on greenhouse warming and carbon-cycle dynamics. *Nature*, *451*, 279–283. https://doi.org/10.1038/nature06588

Zachos, J. C., Pagani, M., Sloan, L., Thomas, E., & Billups, K. (2001). Trends, rhythms, and aberrations in global climate 65 ma to present. *Science*, *292*(5517), 686–693. https://doi.org/10.1126/science.1059412

Zachos, J. C., Röhl, U., Schellenberg, S. A., Sluijs, A., Hodell, D. A., Kelly, D. C., et al. (2005). Rapid acidification of the ocean during the Paleocene-Eocene thermal maximum. *Science*, *308*(5728), 1611–1615. https://doi.org/10.1126/science.1109004

Zachos, J. C., Schouten, S., Bohaty, S., Quattlebaum, T., Sluijs, A., Brinkhuis, H., et al. (2006). Extreme warming of mid-latitude coastal ocean during the Paleocene-Eocene thermal maximum: Inferences from $TEX_{86}$ and isotope data. *Geology*, *34*(9), 737–740. https://doi.org/10.1130/G22522.1

Zachos, J. C., Wera, M. W., Bohaty, S., Delaney, M. L., Petrizzo, M. R., Brill, A., et al. (2003). A transient rise in tropical sea surface temperature during the Paleocene-Eocene thermal maximum. *Science*, *302*(5650), 1551–1554. https://doi.org/10.1126/science.1090110

Zeebe, R. E., & Lourens, L. J. (2019). Solar system chaos and the Paleocene–Eocene boundary age constrained by geology and astronomy. *Science*, *365*(6456), 926–929. https://doi.org/10.1126/science.aax0612

Zeebe, R. E., & Zachos, J. C. (2013). Long-term legacy of massive carbon input to the Earth system: Anthropocene versus Eocene. *Philosophical Transactions of the Royal Society A: Mathematical, Physical and Engineering Sciences*, *371*(2001). https://doi.org/10.1098/rsta.2012.0006

Zeebe, R. E., Zachos, J. C., Caldeira, K., & Tyrrell, T. (2008). Carbon emissions and acidification. *Science*, *321*(5885), 51–52. https://doi.org/10.1126/science.1159124

Zeebe, R. E., Zachos, J. C., & Dickens, G. R. (2009). Carbon dioxide forcing alone insufficient to explain Palaeocene-Eocene thermal maximum warming. *Nature Geoscience*, *2*, 576–580. https://doi.org/10.1038/ngeo578

Zhang, Q., Ding, L., Kitajima, K., Valley, J. W., Zhang, B., Xu, X., et al. (2020). Constraining the magnitude of the carbon isotope excursion during the Paleocene-Eocene thermal maximum using larger benthic foraminifera. *Global and Planetary Change*, *184*, 103,049. https://doi.org/10.1016/j.gloplacha.2019.103049

Zhu, J., Poulsen, C. J., Otto-Bliesner, B. L., Liu, Z., Brady, E. C., & Noone, D. C. (2020). Simulation of early Eocene water isotopes using an Earth system model and its implication for past climate reconstruction. *Earth and Planetary Science Letters*, *537*, 116164 http://doi.org/10.1016/j.epsl.2020.116164